Shape Memory Alloy Actuators for Silicon Microgrippers

Mayra Garcés-Schröder [ORCID], Tom Zimmermann, Carsten Siemers, Monika Leester-Schädel, Markus Böl, and Andreas Dietzel

Abstract—The fabrication of shape memory alloy NiTi actuators by femtosecond laser ablation is presented. Processing parameters are examined and the effect of the ablation process on the shape memory material properties is assessed by electron microscopy and differential scanning calorimetry. It is shown that an efficient ablation process with negligible effect on the shape memory properties of the actuator material has been established with a cutting time of ~3 min per actuator. Two different actuator geometries are studied and their performances are compared by measurements of actuator stroke, force and resistance characteristics. A preconditioning procedure for stabilization of the resistance is presented, permitting an actuator control based on the intrinsic sensor effect. A wafer-level integration process of the actuators into silicon microgrippers is described. [2019-0032]

Index Terms—Femtosecond laser ablation, microgripper microactuator, microfabrication, shape memory alloys.

I. INTRODUCTION

THE use of shape memory materials for the actuation of microsystems can have various advantages over other actuation principles. Shape memory alloys (SMA) feature large stroke, a high work/weight ratio and good scalability [1]. Miniaturization improves the actuator dynamics, since a larger surface/volume ratio favors fast cooling of the devices.

Shape memory actuators are influenced in their performance, transformation temperatures and fatigue progress by a variety of factors including the exact chemical composition, grain size, manufacturing and annealing procedures and loading during operation [2], [3]. This complex behavior poses

great difficulties to developers and calls for the publication of case studies and parameter investigations to build up a knowledge base facilitating the design of SMA-based actuation systems. Reports on foil-based microactuators are particularly rare, as most of the available data was collected on SMA wires for macroscopic systems. Cross *et al.* investigated the differences between different material shapes (wire, foil, rod) and assume that the observed differences arise from different effects of the annealing procedure due to the different geometries of the samples [4].

The integration of SMA actuators in microsystems is challenging. NiTi, which is the most commonly used SMA due to its favorable properties like a large shape memory effect and comparatively high long-term stability [5], is difficult to connect to other materials [6], [7]. Its heat sensitivity on the one hand and the often-high operating temperatures on the other hand complicate the connection with typical materials used for microfabrication. For this reason, there are only a few reports in the literature on the use of SMA for micro-electro-mechanical systems (MEMS) that can be fabricated on wafer level.

Femtosecond laser ablation has in recent years been successfully used as a versatile method for fabricating systems in foil [8]–[10], realizing microfluidic devices, and also as part of sensor fabrication on silicon wafers [11]–[16].

Femtosecond laser ablation can reduce the heat-affected zone in the structured material. Due to the short duration of femtosecond laser pulses, cumulative effects of energy deposition in the processed material can be avoided. Huang *et al.* have identified a redeposited layer of 7 μm thickness and a heat-affected zone of < 70 μm thickness for NiTi [17]. For the ablation of NiTi, two regimes have been described by Uppal and Shiakolas [18]: Ablation with low fluence values of $0.16 - 0.22$ J/cm^2 yields high precision and is termed gentle ablation. The second regime (strong ablation) with threshold fluences of $0.75 - 1.16$ J/cm^2 leads to more thermal damage, but allows high material removal rates. The material removal mechanism likely includes phase explosion in this case.

Here we present an approach for femtosecond laser assisted fabrication of planar SMA microactuators and their integration in silicon microgrippers at wafer level. The parameters for the laser foil cutting process are studied with respect to thermal damage to the substrate material. The manufactured actuators are characterized regarding actuator stroke, force and resistance. The integration process of the actuators in the silicon microgrippers is described.
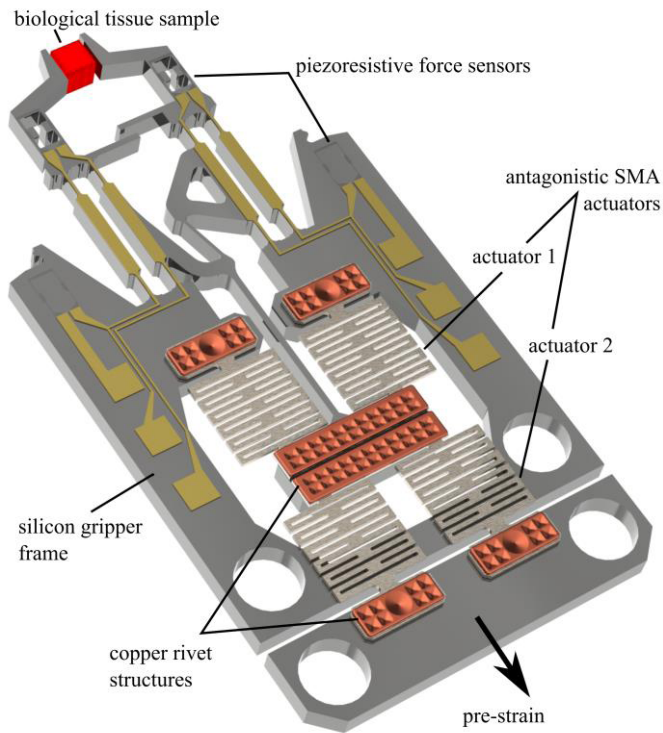
Fig. 1.   Model of the microgripper with piezoresistive force sensors and shape memory alloy actuators.

Our aim was the development of a force-sensitive microgripper with large stroke for the mechanical characterization of biological tissues. A more detailed description of the application and related studies have been published previously [19]–[21].

After a brief introduction of the microgripper concept, the interaction of a femtosecond laser with the NiTi material is described and a parameter set for actuator fabrication is determined. The influence of the fabrication process is then studied by differential scanning calorimetry (DSC). Different actuator geometries are compared regarding homogeneity of resistive heating, stroke, output force and input power. At last, a description of the microgripper fabrication process including the actuator integration is given.

II. MICROGRIPPER CONCEPT

The gripper is designed as an in-plane silicon microsystem with piezoresistive force sensing elements and a double crank gear as described in [22], [23]. A model of the system is shown in Fig. 1. The work is based on a previous process for the production of microgrippers [24], [25].

The grippers are actuated by a pair of antagonistically functioning SMA actuators. Each actuator element has a planar double spring geometry and the two actuators are alternately heated by applying a current. The riveting process mechanically connecting the SMA actuators to the silicon grippers described by Hoxhold [26] has been transferred to standard silicon wafers as opposed to the silicon on insulator (SOI) wafers used before and takes place directly on the silicon

microgripper without a manual assembly of single actuators and grippers.

The actuators need to be pre-strained before the memory effect is available for gripper actuation. To this end, the gripper is mounted in a holder designed to connect it to the necessary periphery for actuator activation and sensing. The holder is equipped with a slide displaced by a micrometer screw. The main gripper body is fixed on the immobile part of the holder and the smaller silicon part connected to the ends of actuator 2 (see Fig. 1) is fixed on the slide. The slide is then moved, enlarging the distance between the two silicon parts and pre-straining the actuator pair.

III. LASER-CUTTING OF SMA ACTUATORS

Laser ablation defines the removal of material induced by irradiation of the surface [27]. The processing parameters for the femtosecond laser fabrication of the shape memory alloy actuators have been studied with the main objective of avoiding thermal damage to the material while obtaining an efficient ablation process.

The mechanisms involved in the ablation process generally depend on the laser parameters pulse duration, light quantum current density (fluence) and the properties of the ablated material. The fluence can be calculated by using

$$F = \frac{Ep}{\pi \, (\text{Ø}/2)^2} \tag{1}$$

in which the diameter of the laser spot is cut off at the edges [18]. Herein F = fluence (J/cm^2), Ep = pulse energy (μJ) and Ø = focus diameter (μm). The focus diameter of the laser beam has been measured by a beam profiler (Ophir SP928 Camera and LBS-300 BB Attenuator, ND filter) and is 22 μm $\pm$ 4 μm with an ellipticity of 0.956. The measurement error is due to the resolution of the image sensor. The energy of individual laser pulses is used here to indicate the energy induced into the material. For orientation, the pulse energy values for the process parameters obtained during the parameter study are converted into estimated fluence values.

The spatial pulse distance

$$D = \frac{V}{f} \tag{2}$$

indicates the distance between two center points of spots on the substrate that were created by successive laser pulses and can be determined by dividing the scanning speed by the pulse frequency value. Herein V: scanning speed (m/s), f: frequency (Hz), D: pulse distance (m).

The pulse distance determines the cumulative energy deposition into the peripheral areas of the processing zone. For small pulse distances, the areas influenced by the laser beam during the individual shots have a large overlap. Li et al. report that the contours of line patterns become smoother with large pulse distances because less energy dissipates into the surrounding material [28]. According to Quintino et al., small pulse distances of about 0.25 μm lead to molten material due to the high cumulative energy input and consequently to hardening cracks [29]. At large pulse distances of greater

than 5 μm, the outlines of the laser-cut trenches show "scallops" with a periodicity not related to the wavelength, as also described by Li *et al.* [28]. These are termed non-coherent structures with parameters depending on the intensity of the incident beam, the scanning velocity and other factors [30]. The parameter pulse distance was studied here to obtain smooth trench edges.

A. Materials and Methods

A 100 μm (+/- 15 μm) thin cold formed NiTi sheet has been used for this study. Milling, annealing and etching have been carried out by the manufacturer with unknown process parameters.

The laser used is a frequency doubled Yb:KGW solid-state laser (Light Conversion Pharos) with a wavelength of 515 nm, which emits a beam with a Gaussian profile and a diameter of 3.7 mm. The beam is focused on the sample surface with an F-Theta lens with a focal length of 100 mm. The spot is positioned on the sample surface with a galvo scanner (Scanlab Intelliscan 14/RTC 5), which enables high processing speeds of up to 3600 mm/s. The sample is mounted on a micromachining platform (Microstruct-C, 3D-Micromac). The pulse duration is fixed to 227 fs and the repetition rate was set to 100 kHz.

For metallographic analyses, the laser-cut NiTi samples were mounted into steel sample holders and embedded (diameter 40 mm) using SCANDIA Scandiplex® A and B cold-curing, yellow transparent, epoxy mounting resin which ensures excellent sample bonding and provides relatively bubble-free results. Approximately one millimeter of the embedded material was removed manually by grinding (SiC grinding paper size P240) to enable analyses of the laser-cut structures. Afterwards, metallographic cross-sections were prepared by automated water-cooled mechanical grinding (ATM Saphir 550) with SiC grinding papers, size P400 (60 seconds), P800 (90 seconds), P1200 (120 seconds) and P2500 (180 seconds), 5 N force single load, counter run. Polishing has been performed on the same machine (5 N force single load) with 9 μm for 600 seconds, counter run, 6 μm (300 seconds, counter run), 3 μm (300 seconds, counter run) Kulzer NewLam® diamond suspension including lubrication, 1 μm (300 seconds, counter run) MicroDiamant Magnum-Top-Duo diamond suspension including lubrication and Sommer OPS (solution of 50 ml OPS + 10 ml H_2O_2) + distilled water, SiO_2 particles of 0.05 μm diameter, 300 seconds counter run followed by 120 seconds synchronized run, two to three of these seven-minutes-cycles with intermediate ultrasonic cleaning in ethanol until a scratch-free surface was achieved.

Due to an excellent corrosion resistance, chemical decoration of NiTi alloys is challenging, especially, if martensitic microstructures are present. Therefore, several attempts had to be made to identify a suitable solution for the present samples to reveal the microstructure: (1) 100 ml H_2O, 6 ml HNO_3, 3 ml HF (Kroll's reagent), 8 seconds – no effect; (2) 10 ml HF, 30 ml H_2O, 60 ml H_2O_2, 8 – 30 seconds – no effect; (3) 86 ml H_2O, 12 ml H_2O_2, 4,5 ml HNO_3, 5 ml HF, 30 seconds – no effect; (4) 84 ml H_2O, 4 ml HNO_3, 14 ml HF, 10 seconds – no effect; (5) 22 ml HF, 22 ml CH_3COOH, 10 ml HNO_3, 10 seconds – microstructure and grain boundaries visible.

The microstructure of the alloys was analyzed by bright field optical microscopy (ZEISS Imager.M2m) including circular polarized light differential interference contrast imaging (C-DIC). Scanning electron microscopy (SEM - Hitachi TM 3000 and LEO 1550, SE (+ InLense) and BSE detectors) was used for detailed microstructure analyses. Global and local chemical compositions were measured by means of energy dispersive X-ray spectroscopy (EDX).

B. Results

The impact zones of the laser beam on the surface of the actuator material were assessed. Fig. 2 and Fig. 3 show the material modification for single pulses, 10 pulses and 100 pulses at different pulse energy values. As pointed out in Fig. 2, three zones of material modification as described by Uppal *et al.* [18] can be identified. The modification zone contains all visible effects of the irradiation on the sample surface. The ripple zone is described below and features periodic structures on the surface. Above the ablation threshold, material is removed from the center of the impacted zone, defining the ablation zone.

For low pulse energy values, periodic ripple structures are observed on the surface. This phenomenon is called laser-induced periodic surface structures (LIPSS) and has been extensively studied and described in the literature. Its
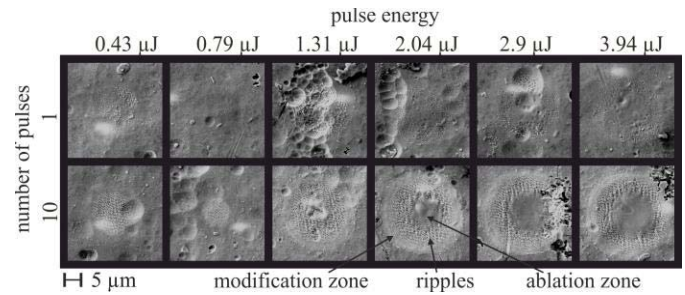

Fig. 2. SEM micrographs of single and 10-fold laser pulse impact zones on NiTi for low pulse energy values.
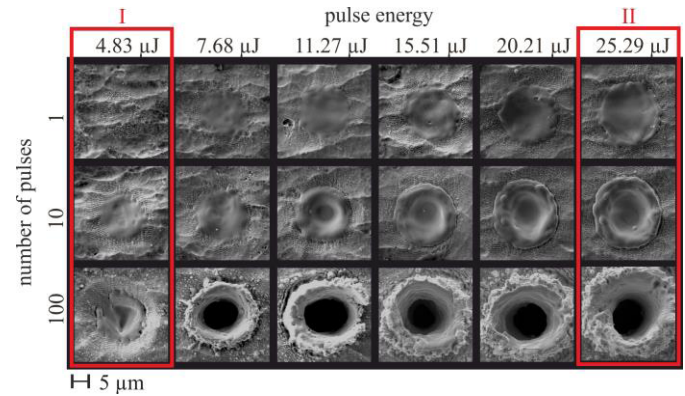

Fig. 3. SEM micrographs of single, 10-fold and 100-fold laser pulse impact zones on NiTi for increasing pulse energy values. The red frames indicate the pulse energy regions for soft ablation (I) and fast ablation (II).
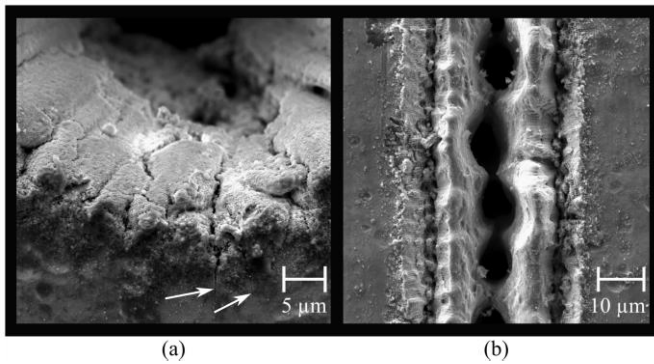
Fig. 4. SEM micrographs of (a) microcracks extending into the bulk material at a pulse distance of 0.01 μm and (b) irregular trench with remaining material connections at a pulse distance of 6 μm.

Fig. 5. Ablation per repetition for different pulse energy values for single path scans at 400 mm/s.

occurrence has been ascribed to the interference of light scattered due to surface defects and the incident beam [30]. Their periodicity is similar to the laser wavelength and their orientation is perpendicular to the laser light polarization [31]. The period of the LIPSS is dependent on the incident angle and the angle of polarization [31]. During ablation tests with 10 pulses per spot we have determined an average LIPSS spacing of ∼870 nm for the fundamental wavelength of 1030 nm of the laser system and of ∼370 nm for the second harmonic wavelength of 515 nm. Those values fit the description of LIPSS reported elsewhere in the literature, e. g. [31].

Ablation characteristics in form of a melted zone in the impact zone center are observed above 1 μJ, superseding the LIPSS in the center of the laser-modified zone. This becomes obvious when comparing the 10-fold pulse incidents. For increasing pulse energy values, the diameter of the ablated region increases. Another change in observed characteristics occurs at approximately 7 μJ. Here a crater forms in the impact zone center and substantial amount of material has been liquefied and removed by evaporation with a rim of recast material left remaining along the edge of the ablation zone. The appearance of the interaction zone and the pulse energy values coincide well with the regime of strong ablation described by Uppal et al. [18].

Pulse distance was varied between 0.01 μm and 5 μm. For low pulse distances of 0.01 μm to 2 μm the rim of the trenches exhibits crack-like structures (see Fig. 4 (a)) that are probably formed due to increased energy deposition, subsequent melting of the material and cracking upon cooling [29]. Trenches cut with large pulse distances above 4 μm feature irregular accumulation of molten material in the trench (see Fig. 4 (b)). A pulse distance of 4 μm is chosen for actuator fabrication, since it allows cutting without cracking of the trench rim. At larger pulse distances, the trenches are not reliably opened and patches of remaining material are observed even at high repetition rates. The pulse distance of 4 μm corresponds to a scanning speed of 400 mm/s. The rate of material removal at this speed for single line scans is shown in Fig. 5 in dependence of pulse energy along with a fit function and the corresponding confidence and prediction bands (95 %). For low pulse energy values up to 5 μJ 100 repetitions of a
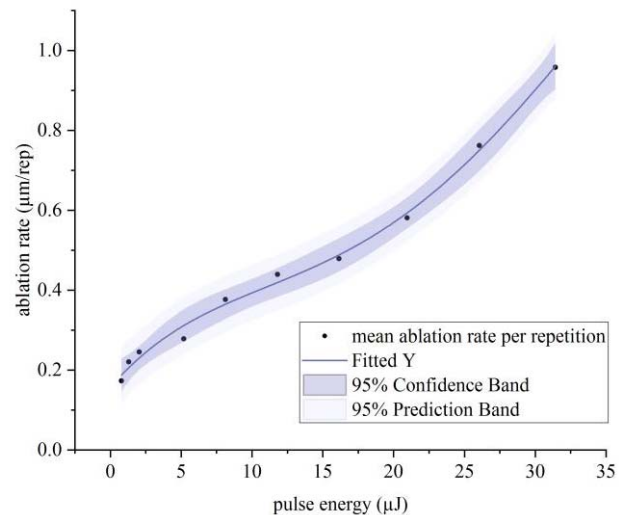
single line scan were made, for higher pulse energy values the number of repetitions was 10. Trench depths were measured by confocal laser scanning microscopy (VK-X260K, Keyence).

Two parameter sets for the femtosecond laser ablation of NiTi were determined after the parameter studies (see red frames in Fig. 3). Both are based on a wavelength of 515 nm, a repetition rate of 100 kHz and a pulse-to-pulse distance of 4 μm:

At low pulse energy of 5 μJ, the zone of thermal damage is negligible. According to the ablation rate presented in Fig. 5, the number of repetitions at this pulse energy necessary to cut through 100 μm of NiTi should only be approximately 500. However, due to recast layers and shadowing of the beam by the upper material edges, the contour would have to be repeated more than 2000 times to cut through the foil. The processing time for a wafer-sized batch of SMA actuators fabricated with these parameters is beyond the acceptable range of few hours.

At higher pulse energy values of around 25 μJ the thermal damage to the material is more pronounced, but the contour repetitions can be reduced to approximately 145 for single line scans. This strategy is applied for actuator fabrication.

The fluence values corresponding to the two strategies can be calculated using Equation (1) and are 1.01 J/cm^2 and 5.09 J/cm^2, respectively. These values are both in the range of strong ablation according to Uppal et al. [18]. These fluence values are only given for rough orientation, since the uncertainties in estimating the spot diameter described above impede a reliable specification.

For many applications, an angle between cutting edge and sample surface of 90° is desired. Due to the profile of the beam, the upper edge of the trench is ablated by the broader part of the beam just above the focal volume, resulting in cropped edges. A solution for this effect described by Li et al. [28] is a modification of the scanning path strategy that consists in scanning several parallel paths for each contour, separated by less than the focal spot radius. The trenches
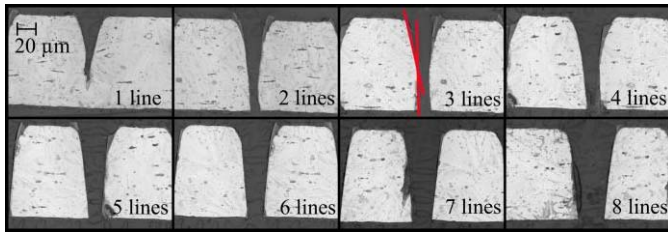
Fig. 6. Bright field optical micrographs of cross-sections of laser-cut trenches with 75 repetitions, 25 μJ pulse energy and 1 to 8 equidistant scanning paths.
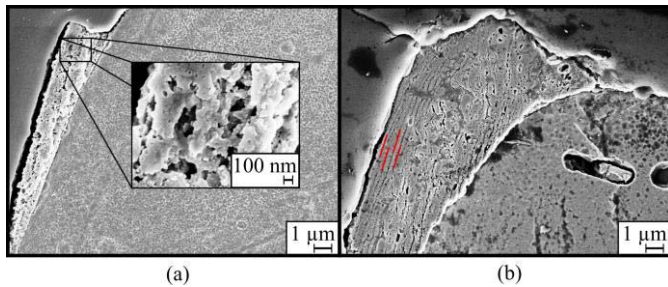

Fig. 7. SEM micrographs of (a) redeposited rim material at cutting edge with porous structure and (b) redeposited oxide at cutting edge, recast layers (red lines).
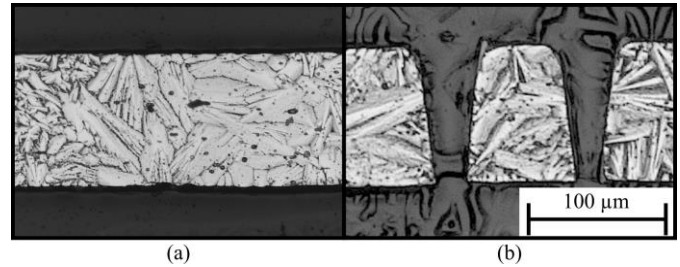

Fig. 8. Light microscopy images of (a) grain structure of reference NiTi sheet and (b) grain structure of NiTi material between laser-cut trenches.
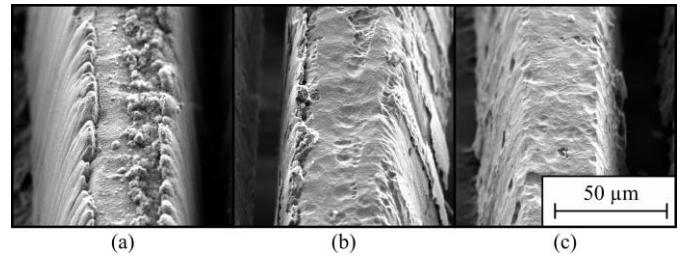

Fig. 9. Laser-cut NiTi foil (a) after laser processing, (b) after 2 min etching, (c) after 5 min etching.

obtained by this strategy are broader than single-path trenches, but yield almost vertical cutting edges. Strategies with varying numbers of equidistant scanning paths have been tested. Fig. 6 shows trenches laser-cut with equidistant scanning paths increasing from 1 to 8 lines with an inter-line distance of 4 μm. For laser-cutting of the actuators, 5 equidistant scanning paths yield reliable results. Due to the narrower kerfs for less equidistant lines, debris and liquefied material cannot efficiently be removed from the kerf during laser-cutting, resulting in residual material at the kerf bottom. For 1 to 4 equidistant lines, the kerf walls exhibit a change of slope as indicated by the red lines in Fig. 6. The kerf walls become increasingly regular for 5 and more equidistant scanning paths.

The microstructure of the material was analyzed after metallographic preparation as described above.

EDX measurements of the matrix material and of the redeposited rim material (see Fig. 7) have been compared in an one-way ANOVA. The mean oxygen fraction in weight-% in the redeposited material was found to be significantly higher than in the matrix material with a mean difference of 22.96 (SE = 1.23), p < 0.001. It is thus concluded that the redeposited layer is oxidized material. This finding is in accordance with [32]. The thickness of the redeposited layer is around 300 nm along most of the kerf walls and rises to few micrometers at the entrance edge of the laser beam.

Haferkamp *et al.* report that the grain structure observed in the studied material is not modified by fs-pulses [33]. In Fig. 8 the grain structure of reference and laser-cut material studied here is shown. No detectable changes to the microstructure occur after femtosecond laser processing.

A short wet etching step after laser cutting was introduced to remove the recast oxide layer. The actuators are etched in 10 ml HF (30 %), 48 ml HNO_3 (65 %) and 128 ml H_2O

for 5 min. Fig. 9 shows images of laser-cut structures before the wet etching (a), after 2 min (b) and after 5 min (c).

IV. CHARACTERIZATION OF THE SMA MATERIAL

One of the most important parameter sets of SMA materials are their transformation temperatures. They are characterized by the start and finish temperatures of the transformation between martensite and austenite during cooling and heating, which differ because of an inherent hysteresis. For some alloys, depending on the production parameters, an additional transformation during cooling is present. It occurs as an intermediate phase between austenite and martensite and has a rhombohedral crystal structure [34].

For an efficient and sustainable operation of the actuators, the knowledge of the transformation temperatures is of great importance. Heating the material in excess of the temperature at which the transformation from martensite to austenite is finished (A_f) results in increased material fatigue and loss of the shape memory effect [35].

There are several established methods for the determination of the transformation temperatures. Two of the most frequently used are differential scanning calorimetry and resistance measurement. Unfortunately, the obtained characteristic transformation temperatures can vary significantly depending on the method employed [2]. This makes comparison of transformation temperatures reported in the literature difficult.

Here we primarily use DSC measurements to investigate the effect of the femtosecond laser treatment on the transformation temperatures.

A. Methods

DSC measurements were carried out in a Mettler Toledo Calorimeter with a heating rate of 10 °C/min. The measurements were started at - 5 °C, the temperature then increased up
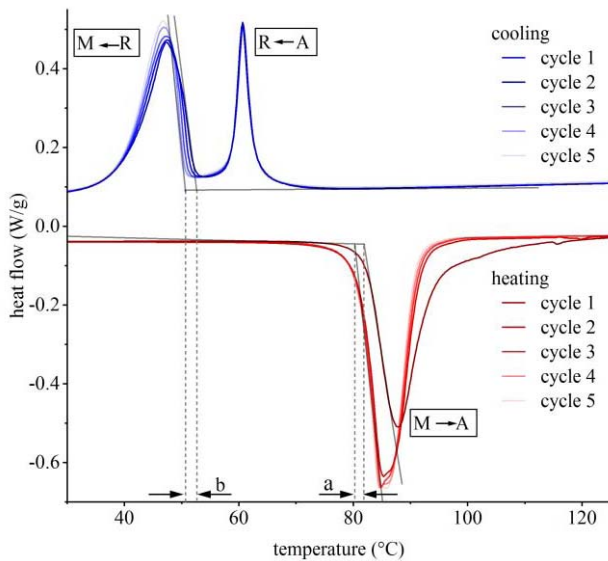
Fig. 10.   DSC measurement of 5 consecutive heating of NiTi (red) and cooling (blue) cycles. (M - martensite; R - rhombohedral phase; A - austenite).

Fig. 11.   DSC measurements (second cycles) for reference and laser-cut material.

to 150 °C and the cycle completed by cooling to - 5 °C again. For temperatures below 200 °C it can be assumed that there is no influence on the properties of the SMA material [36].

To examine the effect of the femtosecond laser machining on the shape memory properties of the NiTi sheet material, two groups of samples were tested. The first group consisted of reference material that was analyzed as received. Rectangular samples were cut from the as-received sheet material with scissors and cleaned in an ultrasonic bath in acetone. The second group consisted of laser-cut actuators (similar to design A introduced below). The parameters optimized for actuator processing were used and the samples were also cleaned as described above. Each group contained $n = 5$ samples.

Peak analysis and statistical testing were carried out with OriginPro and SPSS.

B. Results

To assess the stability of the transformation temperatures during thermal cycling, 5 consecutive DSC cycles were recorded in a first experiment. The start temperatures of the phase transformations were determined using the tangential method. An exemplary recording is visualized in Fig. 10. For the austenite peak during the heating process, a shift towards lower temperatures takes place after the first cycle. After the second cycle, the behavior seems stabilized. Upon cooling, the first of the two peaks (rhombohedral phase) remains stable for all cycles, whereas a shift towards lower start temperatures with each cycle is observed for the second peak (martensite peak). For comparison, the shifts are indicated by dashed lines and the letters *a* (austenite shift) and *b* (martensite shift).

When comparing the mean start temperatures of the three phase changes detected for the first DSC cycle to the ones detected in the second cycle, no significant difference could be found for a significance level of 0.05 in an ANOVA test for any of the sample groups. This is assumed to be
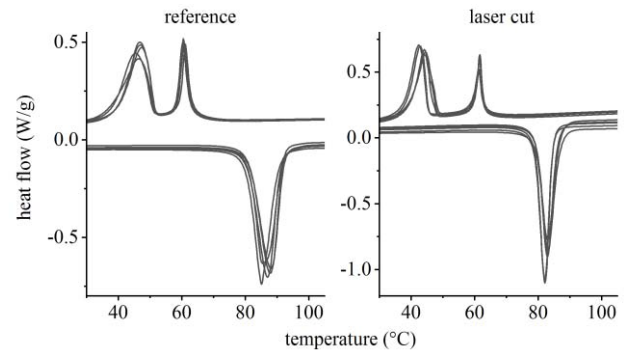
due to the inter-sample variation in start temperatures. The phase transformation start temperature analysis of the first and second DSC cycle for each sample, however, shows that start temperatures generally decrease in the second cycle for the austenite peak and increase for both rhombohedral and martensitic phase peaks.

To account for the shift of the phase change start temperatures, two DSC cycles were conducted for each sample and only the second cycle used for analysis.

The resulting DSC curves for the two groups are shown in Fig. 11. A peak analysis has been performed and a Mann-Whitney-U-test has been carried out for the start temperatures (T_{start}) and full width half maximum (FWHM) of the three phase transformation peaks. The start temperatures of the austenite and martensite peaks showed no significant difference of the mean ranks between reference and laser-cut material. The median of the start temperature for the peak belonging to rhombohedral transformation is decreased by 3 °C after laser cutting. The result of the Mann-Whitney-U-test is U $=$ 0.000, p $=$ 0.008 in this case. The effect strength according to Cohen [37] is r $=$ 0.83 and corresponds to a strong effect. The FWHM of all three transformation peaks differ significantly between reference and laser-cut material. All three peaks are narrower for laser-cut material with a strong effect (r $=$ 0.83) for all three peaks. Fig. 12 shows the confidence intervals (CI) for all transformation peaks and the two indicators T_{start} and FWHM. The data represents a mean value comparison between reference and laser-cut sample groups for visualization of the inter-group differences. Intervals not containing the value 0 indicate a difference between the sample group mean values.

C. Discussion

Regarding the shift of characteristic temperatures between the first and the following DSC cycles, several reports can be found in the literature. An explanation for this behavior is probably a phenomenon termed martensite stabilization. It is observed in cold-rolled NiTi alloys and caused by the deformation of martensite structures during cold-working [38]. The change after the first thermal cycle is presumably caused by relaxation of stress caused by manufacturing and handling.
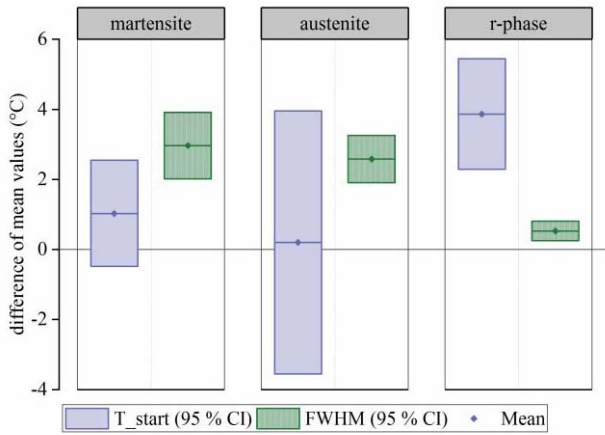
Fig. 12. Confidence interval plot for mean differences of phase change start temperature and FWHM of the DSC peaks of the reference and the laser-cut sample groups.

Kalra *et al.* and Antonucci *et al.* report a decrease in transformation temperatures referring to the comparison between the first DSC cycle and the following ones, whereas Pappas *et al.* observe an increase of austenitic transformation temperature after the first cycle [35], [39], [40]. Abel *et al.* measure transformation temperatures by interpreting displacement-temperature curves and describe a decrease of austenite start temperature and an increase of martensite start temperature with increasing thermal cycle number [41].

The analysis of the DSC measurements of reference and laser-cut material shows no significant modification of the characteristic material properties. The start temperature of the rhombohedral phase is decreased by 5.6 %. However, the rhombohedral phase transformation will later on also be shown to be strongly susceptible to operating and ambient conditions of the actuator elements. The impact of the laser processing on actuator properties is thus negligible.

V. CHARACTERIZATION OF ACTUATORS

Microactuators were laser-cut and characterized regarding stroke, output force and resistance. The effect of a thermal relaxation before actuator operation will be examined and some general effects and considerations regarding the operation parameters will be discussed.

Different actuator designs have been manufactured and characterized to provide tailored solutions for different applications. Design A was adapted from a design developed by Hoxhold for large stroke [26] and an alternative design B for improved temperature and strain distribution was developed. Both designs are shown in Fig. 13.

A. Methods

A custom measurement setup was established for actuator characterization. The measurement setup for force and displacement measurements is shown in Fig. 14. The actuators were soldered to printed circuit boards and those fixed in a custom-made holder. The holder was mounted on a linear
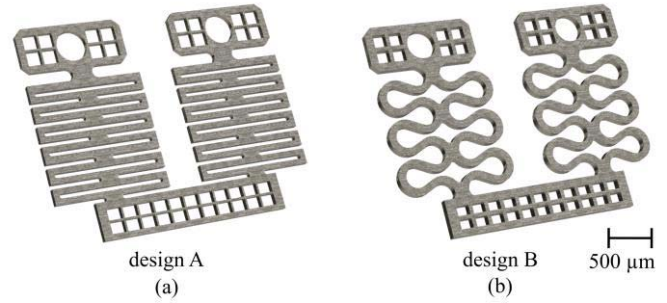

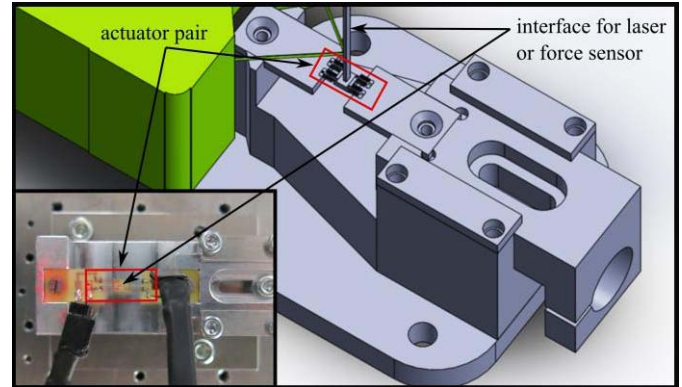Fig. 13. (a) Actuator design A and (b) B.

Fig. 14. Setup for force and displacement measurements. The shown setup is for displacement measurements. For force measurements, only one actuator is integrated and the triangulation sensor (green) is replaced by a force sensor connected to the actuator at the interface.

stage (M-404, Physik Instrumente). A calibrated force gauge (KD78 500mN, ME-Meßsysteme) was used for force measurements and a laser triangulation sensor (LK-H052, Keyence) for displacement measurements. During the experiments, the position of the stage and the associated measured force were recorded and subsequently analyzed. The electrical resistance was measured using a four probes setup.

B. Results

1) Preconditioning Procedure and Resistance Measurements: The first characterizations of the actuators regarding input power and generated force revealed a large scattering (differences of up to 63 %) of the maximum force values between actuators (Fig. 15). This might in part be due to thickness variation of the sheet material and processing tolerances of the laser cutting process. Another factor impacting SME properties are internal stresses introduced by manufacturing and handling the material. A preconditioning treatment was examined that consists of applying a power of 350 mW for one minute to the mechanically unloaded actuator. With this treatment, the power-force curves of different actuators became more homogeneous (see Fig. 15). A deviation of ±131.71 mN at 220 mW in the actuators without relaxation treatment is lowered to a deviation of ±38.22 mN at 220 mW. Notably, the start of the transformation is more reproducible than without the treatment and occurs at approximately 50 mW.
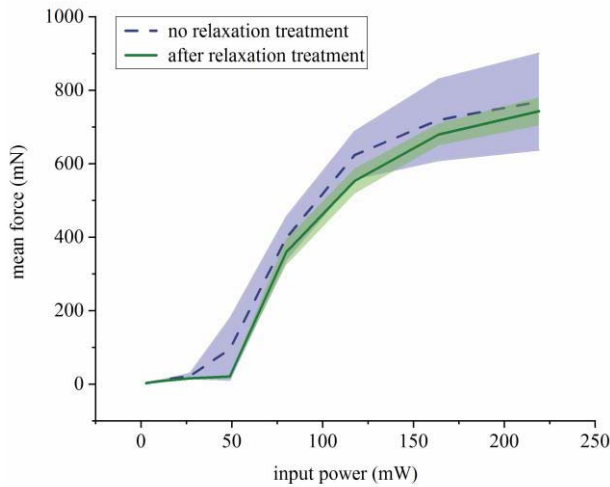
Fig. 15.   Comparison of power-force curves for design A with (n = 5) and without (n = 5) relaxation treatment (350 mW heating power for 1 min).
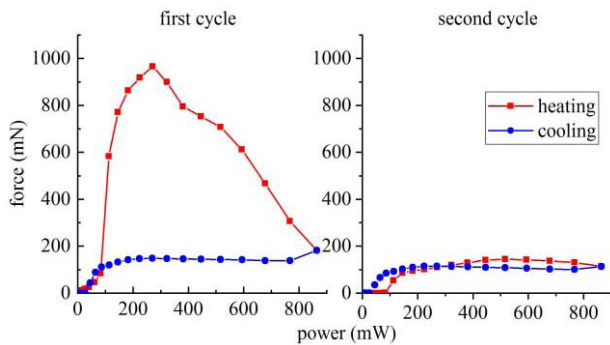

Fig. 16.   Actuator force recording of two cycles with an input power inducing temperatures significantly exceeding A_f (actuator design B, pre-strained by 84%).

Following the determination of the activation power necessary to start phase transformation, a maximum value for the power input for actuator operation was investigated. When a mechanical load is applied to the actuator element, significantly exceeding the A_f temperature leads to a loss of actuation force in the following cycles as demonstrated in Fig. 16. The critical input power has been determined for design A and B (approximately 220 mW) and care was taken not to surpass this value during the following experiments.

Resistance measurements of the actuators are relevant for the detection of the phase transformations needed to implement a control system for efficient operation of the actuators. The effect of the preconditioning procedure can also be observed in the resistance measurements as described in the following.

In Fig. 17, an exemplary preconditioned actuator (900 mW for 1 min) is compared to an exemplary untreated actuator, both without pre-straining. The first and the 20th thermal cycle are shown for both actuators. After preconditioning, the resistance at room temperature is stable. There is still a drift of the high-temperature resistance, but the initial resistance value is restored after each thermal cycle. In the heating part
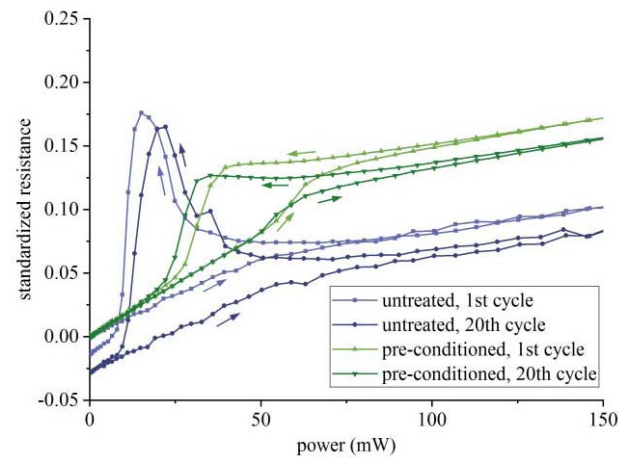

Fig. 17.   1st and 20th thermal cycle for actuator (design B) with and without preconditioning. The resistance is scaled to the first recorded value at room temperature for comparability.
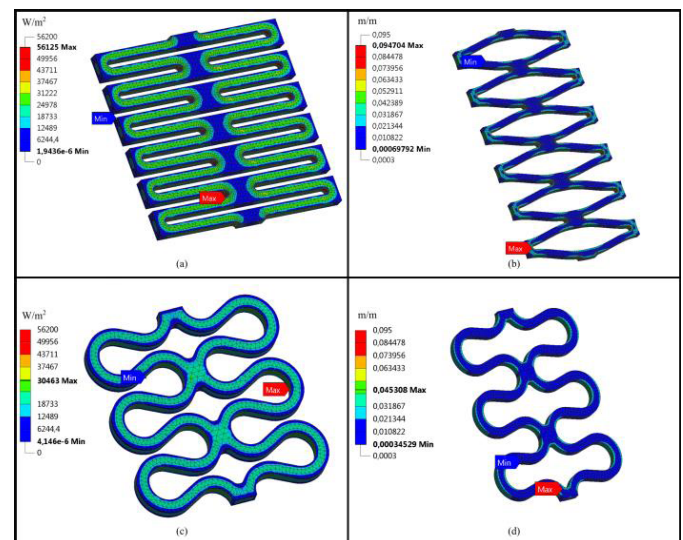
Fig. 18.   Thermal-electrical and mechanical finite element method (FEM) simulation of both actuator designs. (a) and (c) are thermal-electrical analyses, (b) and (d) mechanical strain simulations (5 N force applied to one end of the actuator).

of the measurement, start and end of the phase change of the material from martensite to austenite are detectable by a change in the slope of the curve at approximately 60 mW. The untreated actuator shows an overall drift of the resistance curve to lower values and the phase change during heating is not clearly visible.

2) Actuator Design Comparison: Both actuator designs introduced above were simulated with ANSYS Workbench 18.0 in a stationary thermal-electrical analysis assuming an ambient temperature of 22 °C. The resulting distributions of heat flux density (W/mm²) are visualized in Fig. 18. The distribution is more homogeneous for design B, ensuring that large portions of the actuator material are activated and contribute to the shape memory effect. In design A, the points of maximum heat flux density are overheated when the bulk of the material reaches activation temperature. This also applies to the

Fig. 19. Maximum generated actuator force for different pre-strain levels for actuator design A (a) and B (b).

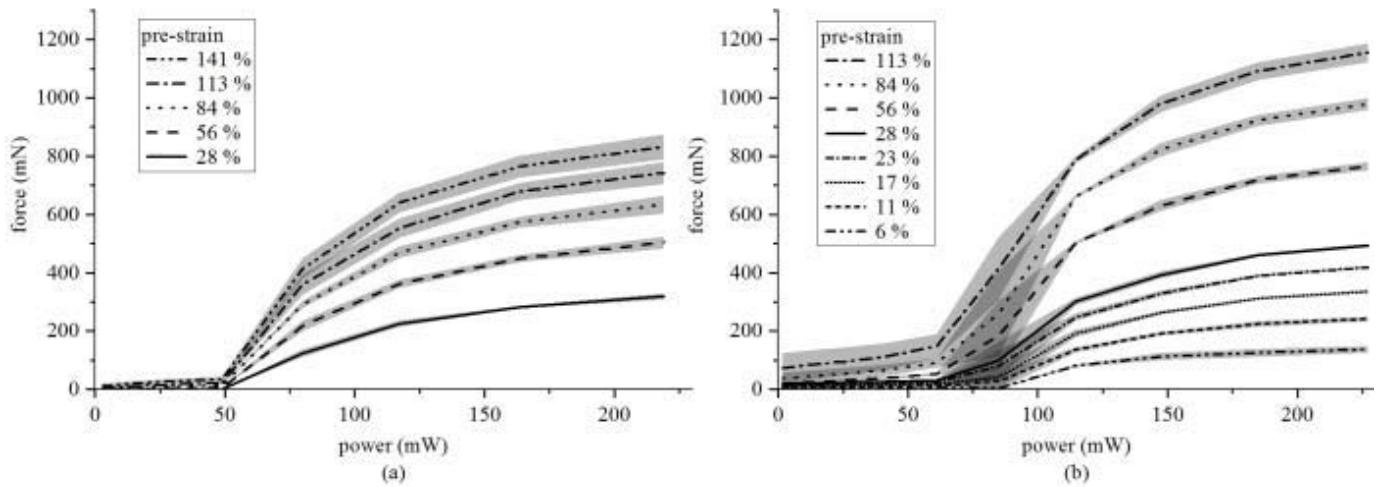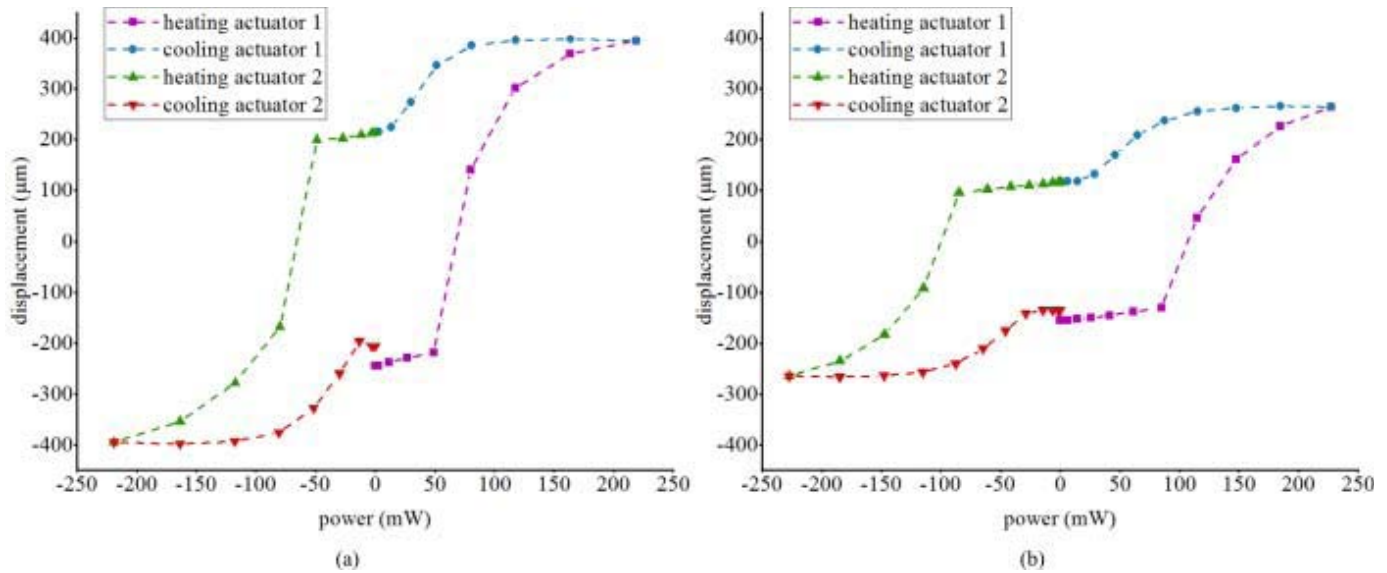Fig. 20. Displacement measurement of one complete cycle of agonist-antagonist actuation for (a) design A and (b) design B.

mechanical stress distribution. The maximum stress upon deformation forms in the inner curvatures of the single lamellar elements and reaches peak values exceeding the maximum recovery stress before the bulk material even enters the strain levels necessary to activate the shape memory effect. This causes the formation of cracks and unrecoverable distortions of the crystal lattice, resulting in increased fatigue. In design B, the strain distribution is more homogeneous, providing larger quantities of strained material available for actuation.

Fig. 19 shows the maximum actuator forces generated depending on the input power and the actuator pre-strain. The maximum forces increase with pre-strain. Design A yields maximum actuator forces of ∼800 μN, the maximum forces for design B are ∼1150 μN.

Fig. 20 shows a power-displacement measurement of a pair of actuators for both actuator versions. The actuator pairs were mounted in the actuator holder and pre-strained by 84%. A full actuation cycle consisting of heating one actuator, waiting for it to cool down, heating the second actuator and again waiting

for it to cool down, has been recorded. The shown actuator pair of design A has a stroke of 800 μm, for design B the maximum stroke is 550 μm.

C. Discussion

It is well known that annealing has a large influence on the shape memory properties of SMA. Langbein and Czechowicz also studied a thermal conditioning treatment for SMA material [5]. They configure wire samples in an oven at temperatures ranging from 300 to 700 °C for 5 min. They found that even short periods of thermal stress application influence the phase transformation temperatures, the shape of the stress plateau in stress-strain curves, the magnitude of the plateau stress, the magnitude of the shape memory effect, the efficiency and the temperature stability of the effect. They reported that transformation temperature intervals decrease for increasing conditioning temperature and time. According to Langbein and Czechowicz, crystal lattice modifications such as the healing of

dislocations occur at temperatures above 250 °C. It was not possible to measure the exact actuator temperatures during preconditioning or experiments described here, but it was ascertained that pre-conditioning takes place at temperatures above 250 °C by measurements with a thermographic camera. The effect observable in Fig. 15 might thus be attributed to relaxation of crystal tensions introduced by manufacturing, processing and handling of the material. Fig. 17 reveals a change in resistivity characteristic after 20 cycles. The long-term stability of the preconditioning effect remains to be studied in future experiments. As reported by Uchil *et al.*, transformation temperatures and resistivity values stabilize after a critical number of thermal cycles that depends on the heat treatment temperature [42]. In their study, peak resistivity is found to be stable after a maximum of approximately 50 cycles.

For a fundamental explanation of resistance curve interpretation, the reader is referred to the literature ([2], [4], [40] for SMA with rhombohedral phase manifestation). During cooling of the material, an increase in resistivity of more than 13% is observed, confirming the presence of the rhombohedral phase [43]. There is no plateau at the maximum value of the resistivity curve, which is assumed to be a sign for a low quantity of rhombohedral phase material by Urbina *et al.* [2]. In this case, it is supposed that a simultaneous transformation of austenite to rhombohedral phase and martensite takes place during cooling.

From the plots in Fig. 17 it can be observed that the phase change upon heating becomes evident after preconditioning and the large increase in resistivity in the cooling part of the plot attributed to the occurrence of the rhombohedral phase is reduced in amplitude. The modification of the resistance behavior during heating is highly advantageous with respect to a control algorithm based on the course of resistance, since the end of the phase transformation can be detected and overheating can be avoided.

The actuator characterization shows an example for tailoring of actuator properties for different requirements. The heat flow and stress distribution in the actuator material have to be carefully considered.

VI. FABRICATION OF SILICON MICRO-GRIPPERS AND WAFER-LEVEL ASSEMBLY OF GRIPPERS AND ACTUATORS

The fabrication process of the microgrippers and the integration of the actuators at wafer level are illustrated in Fig. 21.

The fabrication can be divided into several subprocesses. The first one is the integration of the piezoresistive elements for force sensing (a). A n-doped silicon wafer is coated with a thermal oxide, which is then structured by lithography. A layer of boron-containing liquid (Borofilm100, Emulsitone Chemicals, LLC., USA) is spin-coated onto the wafer top side.

During the following diffusion process at 900 °C for 30 minutes, the boron atoms diffuse into the silicon. The silicon oxide layer is removed by wet-etching in hydrofluoric acid (HF) and a new silicon oxide is deposited. The process of structuring and boron diffusion is repeated to highly dope the contact areas. The oxide is again removed and a third silicon
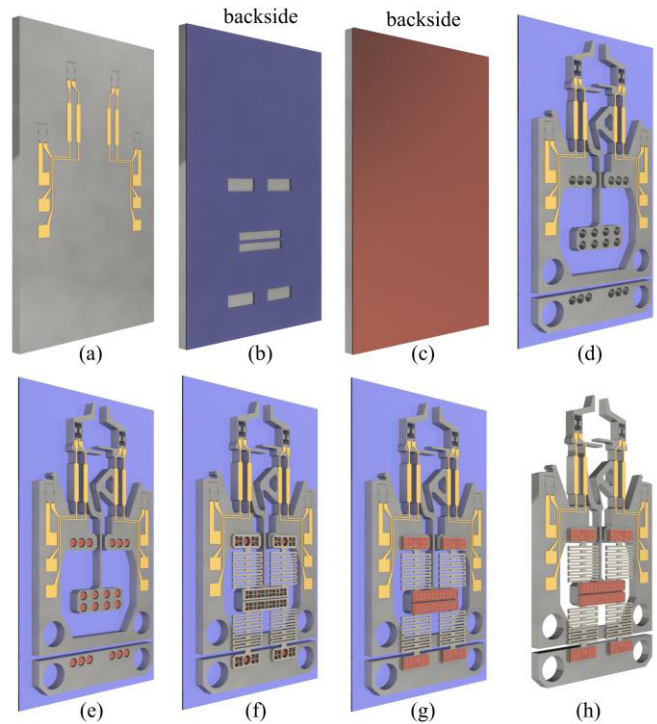

Fig. 21. Fabrication process for silicon microgrippers with piezoresistive force sensors and NiTi actuators.

oxide layer deposited and structured, only leaving open the contact pads of the piezoresistive paths. The silicon oxide layer simultaneously deposited on the wafer backside is protected by a resist layer. Gold conductors are manufactured by sputter deposition and lithography and isolated by a silicon nitride layer.

The backside silicon oxide layer is then structured with openings only at the sites of later copper rivets (b). It is coated with 2 μm copper in a physical vapor deposition process (LS 440 S, Ardenne Anlagentechnik) which serves as a barrier for the reactive ion etching (RIE) of silicon, as a stabilization membrane for the wafer after the microgripper contours have been etched over the entire wafer thickness and as a start layer for copper electroplating (c).

The top side of the wafer is coated with photoresist, which is then photolithographically structured to serve as a mask for the RIE process. The gripper shape and sacrificial structures ensuring constant trench widths for the dry etching process are defined with this mask pattern.

First, the silicon nitride passivating the silicon and conductor paths is etched with this resist mask in a barrel etcher. The RIE process is hereafter performed in a dry etching unit (STS Multiplex, STS), see (d).

The wafer is mounted in a holder with the backside sealed and the front side exposed to an electrolyte. Copper is deposited at the sites at which the backside silicon oxide layer was removed and the backside copper membrane is accessible. The through-holes in the silicon intended for the copper rivets are thus filled with copper until the front surface level is reached, see (e).

The laser-structured NiTi foil is sputter-coated with titanium and copper and electroplated with a negative 3D photoresist
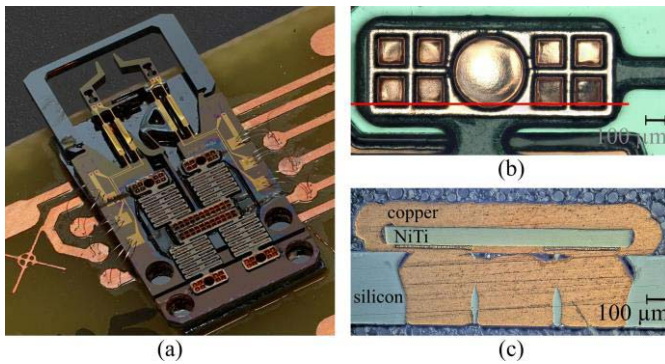
Fig. 22. (a) Microgripper with SMA actuator mounted on a printed circuit board and force sensors contacted by wire bonds for force sensor characterization; (b) Micrograph of rivet connection of gripper and actuator. The red line indicates the approximate position of the cross section shown in (c); (c) Cross section of rivet connection.
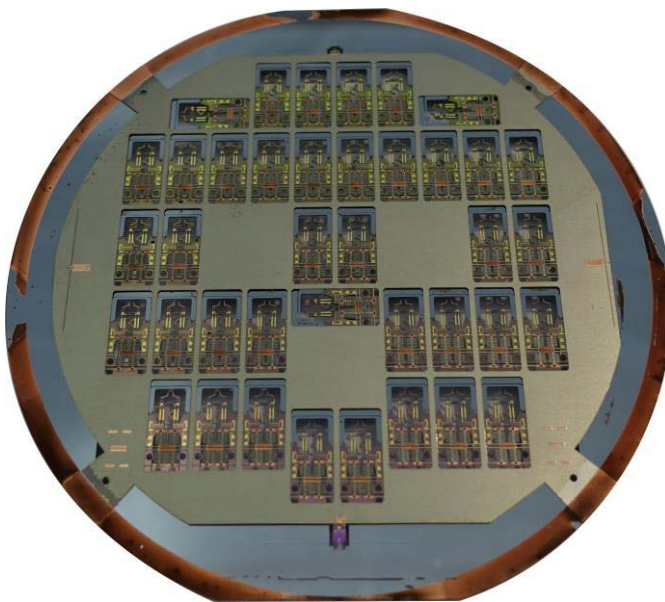

Fig. 23. Silicon wafer (100 mm diameter) with microgrippers and SMA actuators.

(INTERVIA™ 3D-N, Dow). After photolithography on both sides of the foil with different mask designs, the remaining photoresist areas on the bottom side of the actuator foil serve as adhesive to temporarily fasten the SMA actuators to the silicon wafer. To this end, the wafer and the actuator foil are aligned in a mask aligner (EVG) and the stack heated to 90 °C and then cooled to room temperature while wafer and substrate are pressed together (f).

Another electroplating step follows that fills the remaining gap between gripper body and actuators and connects both parts by material and form closure (g). Fig. 22 (b) and (c) show a top view and cross section of the rivet connection, respectively.

In a last step, the copper membrane is etched and the NiTi bridges connecting the actuators in the wafer-sized mesh are laser-cut, releasing the single microgrippers (h). In Fig. 23 a wafer is shown after etching the backside copper and silicon dioxide membranes. The copper rivets are also etched during this step, but since their thickness largely exceeds that of the backside membrane, the functionality is not impaired.

The silicon grippers only remain attached by NiTi bridges forming the actuator mesh.

The released gripper is then mounted on a printed circuit board (PCB), the force sensor contact pads are wire bonded to leads on the PCB and the SMA actuator is contacted by soldering to the PCB. Fig. 22 (a) shows a microgripper after force sensor connection.

VII. Conclusion

Processing parameters and interaction of femtosecond laser radiation on a NiTi surface have been studied and two parameter regimes have been suggested for very gentle (< 1 μJ) and for efficient ($\sim$25 μJ) material removal.

Laser-cut kerfs and actuator samples have been examined by differential scanning calorimetry and electron microscopy and it was found that the detrimental effects of femtosecond laser ablation on both the microstructure of the material and the shape memory characteristics are not significant. The foil material of 100 μm thickness can be cut with almost-vertical kerf walls and a minimal heat-affected zone. The cutting process for one wafer-sized batch (100 mm diameter) including 39 actuator pairs lasts approximately 4 hours, resulting in a cutting time per actuator of approximately 3 min.

SMA actuators have been characterized and two design variants compared concerning actuator stroke and force output. Since the main mechanism causing transformation fatigue in SMA is the accommodation of martensite substructures within the unoriented state under constrained mechanical conditions when A_f is exceeded during cycling [35], [44], it is of great importance to implement a control during actuation. To this end, the resistance of actuators during operation has been analyzed in preparation of the use of the self-sensing capabilities of the NiTi material. As a consequence of these analyses a control algorithm appears feasible on basis of the resistance measurement, which can ensure that temperature is no further increased after reaching the point of complete phase transition to avoid fatigue and loss of force generation ability of the material.

A novel wafer-level assembly process for in-plane shape memory alloy actuators and silicon micro-grippers has been developed. This process enables reliable manufacturing and in-plane operation of the actuators, reducing reject rate by replacing manual assembly. A defined pre-strain of the actuators is introduced during the process of mounting the grippers to a holder and connecting it to energy supply and macroscopic handling devices and can be transferred to wafer-level in the future.

The results obtained in this research show that processing, assembly and also actuator initialization (and training) of hybrid SMA on silicon MEMS is possible at wafer level. This is an important result also for potential high-throughput manufacturing of such hybrid devices.

REFERENCES

[1] B. Winzek *et al.*, "Recent developments in shape memory thin film technology," *Mater. Sci. Eng., A*, vol. 378, nos. 1–2, pp. 40–46, 2004. [Online]. Available: https://linkinghub.elsevier.com/retrieve/pii/S0921509303015168

[2] C. Urbina, S. De la Flor, F. Gispert-Guirado, and F. Ferrando, "New interpretation of the electrical resistivity measurements for obtaining NiTi SMA stress-free transformation temperatures," in *Proc. ASME 11th Biennial Conf. Eng. Syst. Design Anal.*, Nantes, France, 2012, pp. 539–545.

[3] G. Eggeler, E. Hornbogen, A. Yawny, A. Heckmann, and M. Wagner, "Structural and functional fatigue of NiTi shape memory alloys," *Mater. Sci. Eng., A*, vol. 378, nos. 1–2, pp. 24–33, 2004. [Online]. Available: https://linkinghub.elsevier.com/retrieve/pii/S0921509303015144

[4] W. B. Cross, A. H. Kariotis, and F. J. Stimler. (1969). Nitinol Characterization Study. NASA, Washington, DC, USA. Accessed: Nov. 11, 2018. [Online]. Available: https://ntrs.nasa.gov/archive/nasa/casi.ntrs.nasa.gov/19690026989.pdf

[5] S. Langbein and A. Czechowicz, *Konstruktionspraxis Formgedächtnistechnik*. Wiesbaden, Germany: Springer, 2013.

[6] M. Kohl, H. Ossmer, M. Gueltig, and C. Megnin, "SMA foils for MEMS: From material properties to the engineering of microdevices," *Shape Memory Superelasticity*, vol. 104, no. 1, pp. 127–142, 2017.

[7] A. Rao, A. R. Srinivasa, and J. N. Reddy, *Design of Shape Memory Alloy (SMA) Actuators*. Cham, Switzerland: Springer, 2015.

[8] R. E. Schmiedt, C. Qian, C. Behr, L. Hecht, A. Dietzel, and M. Sinapius, "Flexible sensors on polymide fabricated by femtosecond laser for integration in fiber reinforced polymers," *Flexible Printed Electron.*, vol. 3, no. 2, 2018, Art. no. 025003. [Online]. Available: http://stacks.iop.org/2058-8585/3/i=2/a=025003?key=crossref.e0796d3cb1bd56ab6c2a0e1ce0446c84

[9] E. Koch and A. Dietzel, "Skin attachable flexible sensor array for respiratory monitoring," *Sens. Actuators A, Phys.*, vol. 250, pp. 138–144, Oct. 2016. [Online]. Available: https://linkinghub.elsevier.com/retrieve/pii/S0924424716304721

[10] R. Mandamparambil, H. Fledderus, G. van Steenberge, and A. Dietzel, "Patterning of flexible organic light emitting diode (FOLED) stack using an ultrafast laser," *Opt. Express*, vol. 18, no. 8, pp. 7575–7583, 2010. Accessed: Sep. 26, 2013.

[11] D. Metz, N. Ferreira, and A. Dietzel, "3D piezoresistive silicon microprobes with stacked suspensions for tailored mechanical anisotropies," *Sens. Actuators A, Phys.*, vol. 267, pp. 164–176, Nov. 2017. [Online]. Available: https://linkinghub.elsevier.com/retrieve/pii/S0924424717307264

[12] M. Schwerter, D. Gräbner, L. Hecht, A. Vierheller, M. Leester-Schädel, and A. Dietzel, "Surface-passive pressure sensor by femtosecond laser glass structuring for flip-chip-in-foil integration," *J. Microelectromech. Syst.*, vol. 25, no. 3, pp. 517–523, Jun. 2016. [Online]. Available: http://ieeexplore.ieee.org/document/7438755/

[13] T. Schulze, K. Mattern, E. Früh, L. Hecht, I. Rustenbeck, and A. Dietzel, "A 3D microfluidic perfusion system made from glass for multiparametric analysis of stimulus-secretioncoupling in pancreatic islets," *Biomed. Microdevices*, vol. 19, no. 3, p. 47, 2017.

[14] A. Al-Halhouli, W. Al-Faqheri, B. Alhamarneh, L. Hecht, and A. Dietzel, "Spiral microchannels with trapezoidal cross section fabricated by femtosecond laser ablation in glass for the inertial separation of microparticles," *Micromachines*, vol. 9, no. 4, p. 171, 2018.

[15] L. Hecht, D. van Rossum, and A. Dietzel, "Femtosecond-laser-structured nitrocellulose membranes for multi-parameter point-of-care tests," *Microelectron. Eng.*, vol. 158, pp. 52–58, Jun. 2016. [Online]. Available: https://linkinghub.elsevier.com/retrieve/pii/S0167931716301320

[16] P. Erfle, J. Riewe, H. Bunjes, and A. Dietzel, "Optically monitored segmented flow for controlled ultra-fast mixing and nanoparticle precipitation," *Microfluidics Nanofluidics*, vol. 21, no. 12, p. 179, 2017. [Online]. Available: http://link.springer.com/10.1007/s10404-017-2016-2

[17] H. Huang, H. Y. Zheng, and G. C. Lim, "Femtosecond laser machining characteristics of Nitinol," *Appl. Surf. Sci.*, vol. 228, nos. 1–4, pp. 201–206, 2004. [Online]. Available: https://linkinghub.elsevier.com/retrieve/pii/S0169433204000248

[18] N. Uppal and P. S. Shiakolas, "Micromachining characteristics of NiTi based shape memory alloy using femtosecond laser," *J. Manuf. Sci. Eng.*, vol. 130, no. 3, 2008, Art. no. 31117. [Online]. Available: http://ManufacturingScience.asmedigitalcollection.asme.org/article.aspx?articleid=1452068

[19] M. Garcés-Schröder, L. Hecht, A. Vierheller, M. Leester-Schädel, M. Böl, and A. Dietzel, "Micro-grippers with femtosecond-laser machined in-plane agonist-antagonist SMA actuators integrated on wafer-level by galvanic riveting," *Proceedings*, vol. 1, no. 4, p. 385, 2017. [Online]. Available: http://www.mdpi.com/2504-3900/1/4/385

[20] M. Garcés-Schröder, L. Hecht, R. Iyer, M. Leester-Schädel, M. Böl, and A. Dietzel, "Characterization of skeletal muscle passive mechanical properties by novel micro-force sensor and tissue micro-dissection by femtosecond laser ablation," *Microelectron. Eng.*, vol. 192, pp. 70–76, May 2018.

[21] M. Garcés-Schröder, D. Metz, M. Leester-Schädel, and A. Dietzel, "Micromechanical systems for the mechanical characterization of muscle tissue," *Procedia Eng.*, vol. 120, pp. 849–852, Jan. 2015.

[22] S. Büttgenbach, S. Bütefisch, M. Leester-Schädel, and A. Wogersien, "Shape memory microactuators," *Microsyst. Technol.*, vol. 7, no. 4, pp. 165–170, 2001. [Online]. Available: http://link.springer.com/10.1007/s005420000082

[23] M. Garcés-Schröder, M. Leester-Schädel, M. Schulz, M. Böl, and A. Dietzel, "Micro-gripper: A new concept for a monolithic single-cell manipulation device," *Sens. Actuators A, Phys.*, vol. 236, pp. 130–139, Dec. 2015. [Online]. Available: https://linkinghub.elsevier.com/retrieve/pii/S0924424715301850

[24] S. Bütefisch, V. Seidemann, and S. Büttgenbach, "Novel micropneumatic actuator for MEMS," *Sens. Actuators A, Phys.*, vols. 97–98, pp. 638–645, Apr. 2002. [Online]. Available: https://ac.els-cdn.com/S0924424701008433/1-s2.0-S0924424701008433-main.pdf?_tid=8477aa4a-fd81-4f53-8c98-5534dada4324&acdnat=1524249386_015ecc86f0375dfcf88d894066851e02

[25] B. Hoxhold, M. R. Kirchhoff, S. Bütefisch, and S. Büttgenbach, "SMA driven micro grippers combining piezo-resistive gripping force sensors with Epon SU-8 mechanics," in *Proc. 20th Eurosensors*, 2006, pp. 190–191.

[26] B. Hoxhold, "Mikrogreifer und aktive Mikromontagehilfsmittel mit integrierten Antrieben," Ph.D. dissertation, Institut Mikrotechnik, Technische Univ. Braunschweig, Braunschweig, Germany, 2010.

[27] C. Dowding and A. Borman, "Laser-initiated ablation of materials," in *Laser Surface Engineering: Processes and Applications* (Electronic and Optical Materials), vol. 65, 1st ed., J. Lawrence and D. G. Waugh, Eds. Cambridge, U.K.: Woodhead, 2015, pp. 523–546.

[28] C. Li, S. Nikumb, and F. Wong, "An optimal process of femtosecond laser cutting of NiTi shape memory alloy for fabrication of miniature devices," *Opt. Lasers Eng.*, vol. 44, no. 10, pp. 1078–1087, 2006. [Online]. Available: https://linkinghub.elsevier.com/retrieve/pii/S0143816605001661

[29] L. Quintino, L. Liu, R. M. Miranda, R. J. C. Silva, A. Hu, and Y. Zhou, "Cutting NiTi with femtosecond laser," *Adv. Mater. Sci. Eng.*, vol. 2013, no. 13, pp. 1–4, 2013. [Online]. Available: http://www.hindawi.com/journals/amse/2013/198434/

[30] D. Bäuerle, *Laser Processing and Chemistry*, 4th ed. Berlin, Germany: Springer-Verlag, 2011.

[31] I. Gnilitskyi, T. J.-Y. Derrien, Y. Levy, N. M. Bulgakova, T. Mocek, and L. Orazi, "High-speed manufacturing of highly regular femtosecond laser-induced periodic surface structures: Physical origin of regularity," *Sci. Rep.*, vol. 7, no. 1, 2017, Art. no. 8485. [Online]. Available: https://www.nature.com/articles/s41598-017-08788-z.html

[32] A. Sharma and V. Yadava, "Experimental analysis of Nd-YAG laser cutting of sheet materials—A review," *Opt. Laser Technol.*, vol. 98, pp. 264–280, Jan. 2018. [Online]. Available: https://linkinghub.elsevier.com/retrieve/pii/S0030399216313068

[33] H. Haferkamp, M. Goede, M. Leester-Schaedel, and S. Paschko, "Keeping the shape memory properties of miniaturized components of NiTi alloys by laser machining," *Proc. SPIE*, vol. 3675, pp. 267–274, Jul. 1999.

[34] R. Brammajyosula, V. Buravalla, and A. Khandelwal, "Model for resistance evolution in shape memory alloys including R-phase," *Smart Mater. Struct.*, vol. 20, no. 3, 2011, Art. no. 035015. [Online]. Available: https://ac.els-cdn.com/S0921509399003597/1-s2.0-S0921509399003597-main.pdf?_tid=f4b33bf9-d44c-4866-9809-3bd02048cb57&acdnat=1533307110_0d9dbc6a3139fc03ff8b9dc59b4a9e88

[35] P. Pappas, D. Bollas, J. Parthenios, V. Dracopoulos, and C. Galiotis, "Transformation fatigue and stress relaxation of shape memory alloy wires," *Smart Mater. Struct.*, vol. 16, no. 6, pp. 2560–2570, 2007. [Online]. Available: http://stacks.iop.org/0964-1726/16/i=6/a=060?key=crossref.ce17dd7c7208d9454c1a332ccbe92929

[36] A. Ziółkowski, "On analysis of DSC curves for characterization of intrinsic properties of NiTi shape memory alloys," *Acta Phys. Polonica A*, vol. 122, no. 3, pp. 601–605, 2012. [Online]. Available: http://przyrbwn.icm.edu.pl/APP/PDF/122/a122z3p43.pdf

[37] J. Cohen, "Statistical Power Analysis," *Current Directions Psychol. Sci.*, vol. 1, no. 3, pp. 98–101, 1992. [Online]. Available: http://journals.sagepub.com/doi/10.1111/1467-8721.ep10768783

[38] S. K. Wu, H. C. Lin, and P. C. Cheng, "Multi-strengthening effects on the martensitic transformation temperatures of TiNi shape memory alloys," *J. Mater. Sci.*, vol. 34, no. 22, pp. 5669–5675, 1999. [Online]. Available: http://link.springer.com/10.1023/A:1004757822046

[39] S. Kalra, B. Bhattacharya, and B. S. Munjal, "Design of shape memory alloy actuated intelligent parabolic antenna for space applications," *Smart Mater. Struct.*, vol. 26, no. 9, 2017, Art. no. 095015. [Online]. Available: http://stacks.iop.org/0964-1726/26/i=9/a=095015?key=crossref.a264b21a02ac72c7a9cbf8e09f95e1e3

[40] V. Antonucci, G. Faiella, M. Giordano, F. Mennella, and L. Nicolais, "Electrical resistivity study and characterization during NiTi phase transformations," *Thermochimica Acta*, vol. 462, nos. 1–2, pp. 64–69, 2007. [Online]. Available: https://linkinghub.elsevier.com/retrieve/pii/S0040603107002390

[41] E. Abel, H. Luo, M. Pridham, and A. Slade, "Issues concerning the measurement of transformation temperatures of NiTi alloys," *Smart Mater. Struct.*, vol. 13, no. 5, pp. 1110–1117, 2004.

[42] J. Uchil, K. G. Kumara, and K. K. Mahesh, "Effect of thermal cycling on R-phase stability in a NiTi shape memory alloy," *Mater. Sci. Eng., A*, vol. 332, nos. 1–2, pp. 25–28, 2002. [Online]. Available: http://linkinghub.elsevier.com/retrieve/pii/S0921509301017117

[43] S. K. Wu, H. C. Lin, and T. Y. Lin, "Electrical resistivity of Ti–Ni binary and Ti–Ni–X (X = Fe, Cu) ternary shape memory alloys," *Mater. Sci. Eng., A*, vols. 438–440, pp. 536–539, Nov. 2006. [Online]. Available: https://linkinghub.elsevier.com/retrieve/pii/S092150930600699X

[44] S. Barbarino, E. I. S. Flores, R. M. Ajaj, I. Dayyani, and M. I. Friswell, "A review on shape memory alloys with applications to morphing aircraft," *Smart Mater. Struct.*, vol. 23, no. 6, 2014, Art. no. 063001. [Online]. Available: https://iopscience.iop.org/article/10.1088/0964-1726/23/6/063001/pdf

Carsten Siemers started his research career on the machinability of Titanium alloys as an Early Stage Researcher in Braunschweig in 2000. In 2005, he was a Senior Research Scientist with the University of Technology (TU) Braunschweig, where he currently heads the Titanium Research Group of the Institute for Materials. His research group is focused on the development of advanced Titanium alloys for several fields of applications, such as the aerospace, the medical and the automotive industries, which includes the identification of alloy compositions and alloy production and alloy characterization and testing in laboratory and industrial scale. He has authored and coauthored more than 80 papers in the field of materials science and engineering with more than 450 citations. In 2012, he has been elected as a Chairman of the Titanium Technical Experts' Committee of the German Materials Society (DGM), i.e. a liaison person between Academia and Titanium industry in Germany. This includes the position of the German representative in the international organizing committee of the Titanium World Conference.

Monika Leester–Schädel received the Diploma degree in mechanical engineering and the Ph.D. degree from Technische Universität (TU) Braunschweig, in 1997 and 2004, respectively. Since 1997, she has been with the Institute of Microtechnology (IMT), TU Braunschweig, and since 2013 as an Academic Senior Councilor. Her research interests include the microfabrication based on established and innovative manufacturing technologies, the design and development of micro actuator systems, micro systems for medical engineering, and micro sensors for application in aeronautics and measurement systems.

Markus Böl received the Diploma degree in civil engineering from the Technical University of Dortmund, and the Ph.D. degree from the Ruhr-Universität Bochum in 2005. Since 2007, he has been the holder of a junior professorship with the Technical University of Braunschweig, where he became a Leader of the Institute of Solid Mechanics in 2009. His research focus is the (numerical) multi-scale/multi-field material modeling. Beside traditional materials, he is concerned with more advanced materials, like biofilm, skeletal muscles, or smooth muscles, to list only a few.

Mayra Garcés-Schröder received the Diploma degree in business engineering from the Karlsruhe Institute for Technology (KIT) in 2011. She has been a Research Assistant with Technische Universität (TU) Braunschweig, since 2011. Since 2012, she has been with the Institute of Microtechnology (IMT), TU Braunschweig, where she is currently pursuing the Ph.D. degree. Since 2019, she has been with the Institute of Semiconductor Technology (IHT), TU Braunschweig, as a Group Leader. Her research interests include 3D microfabrication technologies, microsystems for life science applications, and µLED technology.

Andreas Dietzel received the Ph.D. degree in physics from the Institute of Medical Physics and Biophysics, University of Göttingen in 1989.

From 1990 to 2003, he worked for IBM research and development at laboratories of the Microelectronics Division in Böblingen (D), the Research Division in Rüschlikon (CH) and the Storage Systems Division in Mainz (D) where from 1996 to 2003, he was heading a department. In 2003, he joined Robert Bosch Reutlingen (D) as a Project Manager for the base development of acceleration sensors of the 3rd generation. In 2004, he joined the University of Technology in Eindhoven (NL) as a Full Professor for Micro and Nanoscale Engineering. From 2007 to 2011, he was a Program Manager for the TNO Holst Centre System-in-Foil open innovation platform. In 2012, he was appointed as a Full Professor at the Technische Universität Braunschweig and has been the Head of the Institute of Microtechnology. His research focuses on the design and fabrication of MEMS, systems-in-foil, and microfluidic systems with applications in the life sciences.

Tom Zimmermann was born in Merseburg, Germany, in 1990. He received the bachelor's degree in mechanical engineering with a specialization in mechatronics from Technische Universität Braunschweig in 2017, where he is currently pursuing the master's degree. He has been a Student Research Assistant in the fields of optical metrology, micromechanics, and automation engineering.